JSR Publications

Available Online

J. Sci. Res. **15** (3), 739-757 (2023)

JOURNAL OF SCIENTIFIC RESEARCH

www.banglajol.info/index.php/JSR

DFT and DFT+U Insights into the Physical Properties of UO_2

M. Islam*

Nuclear Safety, Security and Safeguard Division, Bangladesh Atomic Energy Regulatory Authority (BAERA), E-12/A, Agargaon, Dhaka-1207, Bangladesh

Received 11 February 2023, accepted in final revised form 26 June 2023

Abstract

This study reports the structural, electronic, magnetic, elastic, thermal, and optical properties of UO_2 solid crystalline material by applying DFT and DFT+U approximation methods. The direct band gap Mott-Insulating electronic properties are found successfully by using both the LDA+U and GGA+U functionals, and the energy band gap values are obtained in the range from 1.725 to 2.860 eV. The XRD and Neutron diffraction peaks confirmed the fcc-structured fluorite type UO_2. UO_2 is found mechanically stable and ductile from elastic constants calculations. The lattice thermal conductivity is 8.8 Wm^{-1} K^{-1} at 323 K, which is very close to the reported theoretical and experimental results. The frequency-dependent optical parameters are calculated from complex dielectric functions, which indicate that UO_2 is simultaneously an efficient absorber and reflector for ultraviolet radiation in particular energy regions. Although UO_2 is a potential fuel material and cannot be used for conventional optical devices, the anisotropic optical properties, higher dielectric constant, and semiconducting electronic property indicate that the radioactive UO_2 exhibits interesting optoelectronic behaviors also.

Keywords: UO_2; DFT+U functional; Mott-Insulator; Optical properties.

doi: http://doi.org/10.3329/jsr.v15i3.64394 J. Sci. Res. **15** (3), 739-757 (2023)

1. Introduction

Nuclear Power Plant (NPP) can play a leading role in producing clean energy without fossil fuel utilization and carbon emission. Uranium Dioxide (UO_2), the other name Urania, is commonly and broadly used as a nuclear fuel material in Nuclear Power Reactor (NPR) to produce thermal energy through the Nuclear Fission Reaction process. This fuel material mostly attracts researchers in the last few decades due to its availability and standard technological applications in the Nuclear Power sector [1-3]. To utilize UO_2 fuel in NPR in an efficient manner, it is very much necessary to know its physical properties well. UO_2 is a black-colored crystalline radioactive material that is generally fabricated from U_3O_8 (Yellow-cake) through several extraction processes.

Density Functional Theory (DFT) and DFT+U (where U means Hubbard U correction parameter) are the most popular and outstanding simulation methods for the calculation/estimation of various physical properties of crystalline materials. UO_2 shows

* *Corresponding author*: m.islam4399@gmail.com

exceptional electronic, thermal, optical, and magnetic properties for the peculiar behavior of the partially filled *5f* band [2]. By applying the general DFT approximation method, using Generalized Gradient Approximation (GGA) and Local Density Approximation (LDA) for the electronic exchange-correlation functional, incorrectly reveals metallic behavior with zero energy band gap (E_g= 0) for UO_2 due to the strong correlation effect between *5f* orbital electrons. A UO2 solid behaves like a semiconductor with an energy gap in band structure known as *f-f* Mott-Insulator [1,2]. For this strong correlation system, Hubbard U correction based on a corrective function from Hubbard Model [3] is needed to investigate the real electronic and magnetic properties of UO_2.

Many researchers investigated structural [1,10,12], electronic [1,2,8,10,12], magnetic [1,11], thermal [4,5,7], and optical [6,8,10] properties of UO_2 through different approximation methods such as LDA [9], LDA+U [1,7,9,12], GGA [8,9], GGA+U [2,4,6,8,10], HSE (Hybrid functional) [1], HSE06 (Hybrid functional) [11] and so on. To the best of my knowledge, no results have been reported so far for the (i) thermal conductivity measurement by Slack's equation from elastic constants calculations, (ii) X-ray diffraction (XRD) and Neutron diffraction patterns theoretically, and (iii) optical band gap calculation by Tauc's Plot Method for UO_2.

Therefore, in this research, the structural, electronic, magnetic, elastic, and thermal (thermal conductivity) properties of UO_2 solid crystalline material were successfully investigated through the GGA, LDA+U, and GGA+U (U= 4.5 and 5.5 eV) electronic exchange-correlation functional methods without applying any Hybrid functional. Also, the optical properties of UO_2 were explored comprehensively.

The outline of this paper is organized as follows: a summary of the computational methodology is presented in Section 2, the computational results and associated analyses are discussed in Section 3, and finally, in Section 4, the findings of this investigation are concluded.

2. Computational Methodology

The crystal structure of UO_2 possesses fluorite (CaF_2) type face-centered cubic (fcc) structure with the space group $Fm\bar{3}m$ and the corresponding number is 225. The ideal structure of stoichiometric UO_2 is described with two sublattices for U^{4+} and O^{2-} ions, respectively. The U^{4+} cations and O^{2-} anions occupied in Wyckoff positions octahedral 4a (0, 0, 0) and tetrahedral 8c (1/4, 1/4, 1/4) in the lattice sites. The conventional unit cell of fcc UO_2 consists of four formula units which have four U^{4+} ions and eight O^{2-} ions. The size and shape of the unit cell are defined by the lattice constant. Generally, a three-dimensional lattice has three mutually perpendicular axes referred to as a, b, and c along the x, y, and z directions. The three-dimensional view of the conventional unit cell of UO_2 is shown in Fig. 1.

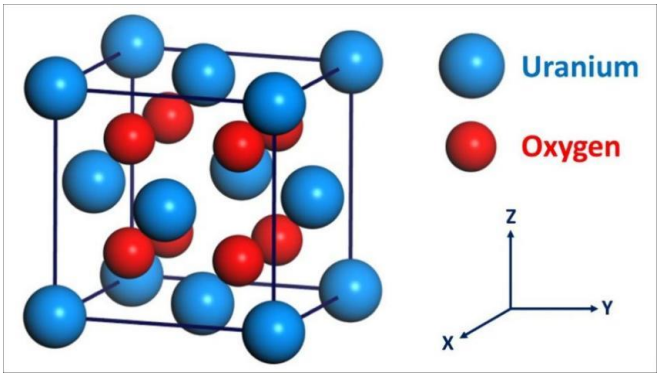

Fig. 1. Three-dimensional conventional unit cell of UO_2 solid crystalline material.

To analyze the structural properties of the ground state configuration of the fcc UO_2, at first, geometry optimization is carried out with zero applied pressure, based on spin-polarized density functional theory (DFT) and DFT+U with Perdew-Burke-Ernzerhof (PBE) and Ceperley-Alder-Perdew-Zunger (CA-PZ) parameterized generalized gradient approximation (GGA) and local density approximation (LDA) functionals as implemented in Cambridge Serial Total Energy Package (CASTEP) code [13]. The main advantage of the DFT+U method is that only the difference of correlation (U) and exchange (J) parameter (U-J) is important. In my work, only one parameter (U) is adjustable [8] due to the implementation of CASTEP code in Materials Studio [8,13]. Here, the values of U are considered as 4.5 and 5.5 eV for the best agreement with the reported results. GGA-PBESOL (PBE for Solids) functional [11] is applied for elastic constants calculations because CASTEP cannot calculate elastic constants with DFT+U functional. Also, Forcite Tools from Materials Studio CASTEP [13] version 8.0 is used to get the X-ray diffraction (XRD) and neutron diffraction patterns for fcc UO_2. k-point sampling within the Brillouin zone (BZ) has been carried out with 5×5×5 k-mesh in the Monkhorst-pack grid scheme [14], which ensures the numerical convergence of all the calculated properties. The cut-off energy for the plane wave expansion is taken as 500 eV for all calculations. The following valence electrons have been considered for U ($6s^2 7s^2 6p^6 6d^2 5f^2$) and O ($2s^2 2p^4$). The Broyden Fletcher Goldfarb Shanno (BFGS) technique was used for relaxation of the geometrical structure, and density mixing was used for electronic structure calculation. The relaxation conditions of UO_2 were: the convergence of the total energy is 1×10^{-6} eV/atom, the maximum force on the atom is 0.03 eV/Å, the maximum ionic displacement is set to 0.001 Å, and the maximum stress of 0.05 GPa. Then the optimized/relaxed unit cell, lattice parameters, and equilibrium volume were obtained from this simulation. The cell parameters of the relaxed structures are listed in Table 1, with other reported results for comparison. It is to be noted that the experimental lattice parameter was obtained at room temperature while the theoretical data by DFT and DFT+U calculations are determined at 0 K.

Table 1. Optimized and experimental structural parameters.

Compound	Method	Lattice constant (Å)			Volume, V $(Å)^3$	Remarks
		a	b	c		
UO_2	GGA	5.475	5.475	5.475	164.095	This work
	LDA+U, U=4.5 eV	5.483	5.483	5.483	164.820	This work
	GGA+U, U=4.5 eV	5.528	5.528	5.528	168.891	This work
	LDA+U, U=5.5 eV	5.502	5.502	5.502	166.565	This work
	GGA+U, U=5.5 eV	5.623	5.623	5.623	177.788	This work
	LDA+U, U= 4.5 eV	5.500	5.500	5.490	-	[1]
	HSE-ACE	5.530	5.530	5.540	-	[1]
	GGA+U, U= 4.5 eV	5.490	5.490	5.490	165.469	[17]
	GGA+U, U= 4.0 eV	5.550	5.550	5.550	170.954	[18]
	Experimental	5.470	5.470	5.470	163.667	[4]
	Experimental	5.471	5.471	5.471	163.757	[16]

From Table 1 it is obvious that UO_2 exhibits fluorite-type fcc structure after the geometrical relaxation of the unit cell with all the LDA, GGA, LDA+U, and GGA+U calculations in the present work. All the physical properties of UO_2 were further calculated from the geometrically relaxed unit cell. The lattice parameter depends on the approximation method and also on the Hubbard U parameter value. The unit cell volumes obtained from the theoretical calculation of different approximation functionals are slightly larger than the experimental values. This improvement is due to considering spin-polarized DFT calculations in the CASTEP code [8,13]. On the other hand, the GGA approximation functionals slightly overestimate the lattice constants due to softening of the electronic orbitals [15].

3. Results and Discussion

3.1. *Structural, electronic and magnetic properties*

The electronic band structure, total and spin density of states (TDOS and SDOS) of the fcc UO_2 optimized with GGA approximation is presented in Fig. 2. Fig. 2(a) shows the electronic energy band structure of fcc UO_2 along the high symmetry directions (X-R-M-Γ-R) of the Brillouin zone at zero pressure in the energy range from -9.0 to +4.0 eV. The band structure calculations show that the valence and conduction bands overlap, and many bands cross the Fermi level. This indicates the metallic nature of fcc UO_2. Due to its metallic nature, UO_2 must have a spin magnetic moment. The moments calculated from the up spin and down spin curve of SDOS, as shown in Fig. 3(b) for UO_2 and U, are tabulated in Table 2. The larger magnetic moment value, μ, is due to the GGA functional application without any Hubbard U correction.

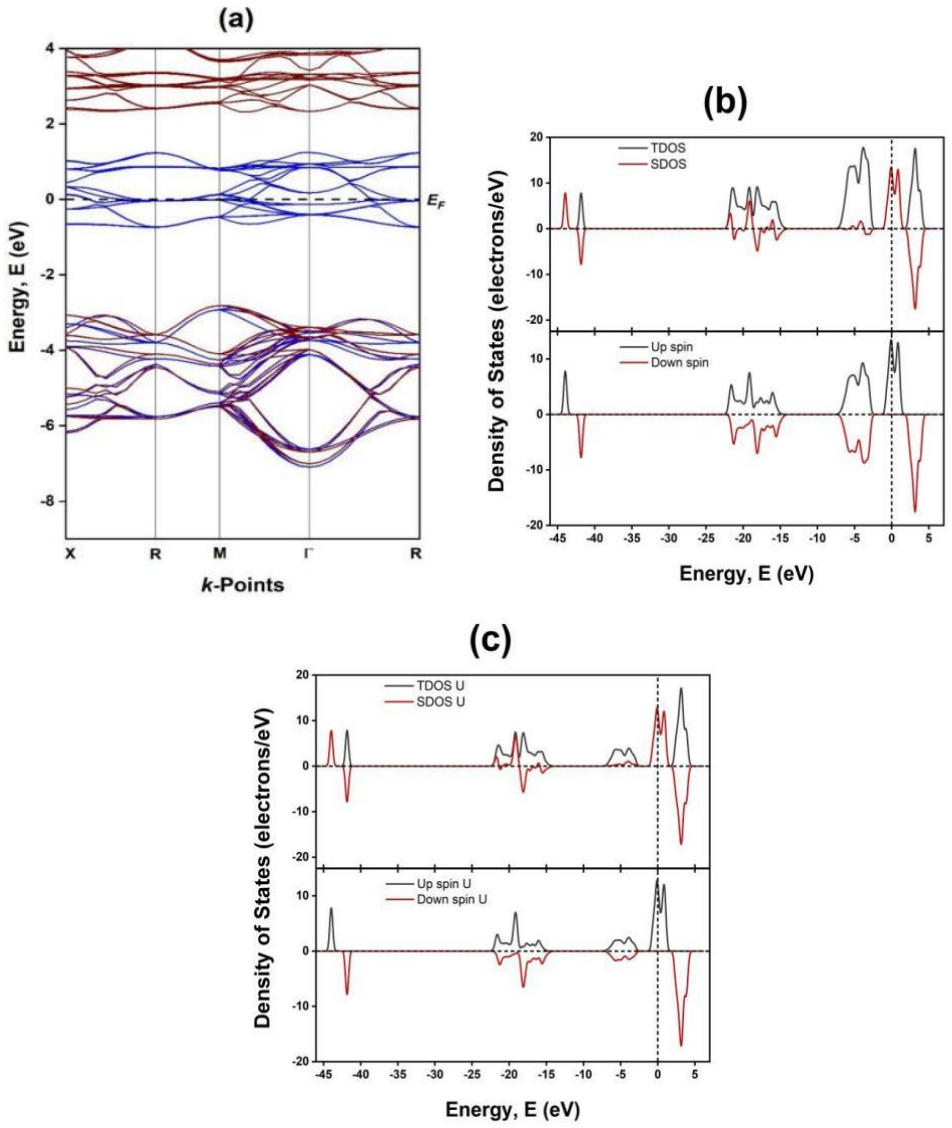

Fig. 2. (a) Energy band diagram, (b) Total and Spin DOS and (c) Total and Spin DOS of U atom of UO_2 with GGA approximation.

Table 2. Spin magnetic moment, μ of UO_2 and U calculated from SDOS value at Fermi level, E_F.

Compound	Method	Number of Formula Units per unit cell of UO_2	Magnetic moment, μ_{total} (μ_B/formula unit)	Magnetic moment, μ_U (μ_B/U atom)	Remarks
UO_2	GGA	4	3.03	2.85	This work
	GGA+U,U= 4.0 eV	4	-	1.89	[2]
	GGA+U,U= 4.0 eV	4	-	1.94	[18]

After Hubbard U parameter correction for strongly correlated *5f* orbital of UO_2, direct band gap semiconducting properties named by Mott-Insulators are found for all the approximation functionals. Fig. 3 shows the electronic energy band structure of fcc UO_2 along the high symmetry directions (X-R-M-Γ-R) of the Brillouin zone at zero applied pressure in the energy range from -9.0 to +4.0 eV for different DFT+U approximation functionals. In DFT+U calculations, I have used the values 4.5 and 5.5 eV for the Hubbard U parameter. The calculated bandgap and E_g values are listed in Table 3 with comparison.

It is seen from Fig. 3 (a) the energy band gap value, E_g= 1.725 eV with the LDA+U (U=4.5 eV) approximation, which is well agreed with the value obtained by Samira Sheykhi *et al.* [1] and F. Gupta *et al*. [18]. The band gap values, E_g= 2.354 eV and 2.051 eV from GGA+U (U= 4.5 eV) and LDA+U (U= 5.5 eV) approximations as shown in Fig. 3(b) and 3(c), respectively are very close to the experimental value (E_g= 2.100 eV) [8]. The larger value of band gap, E_g= 2.860 eV from GGA+U (U= 5.5 eV) approximation functional as shown in Fig. 3(d), is due to the larger value of Hubbard U correction, and this value is in good agreement with the value obtained by Singh *et al.* [10].

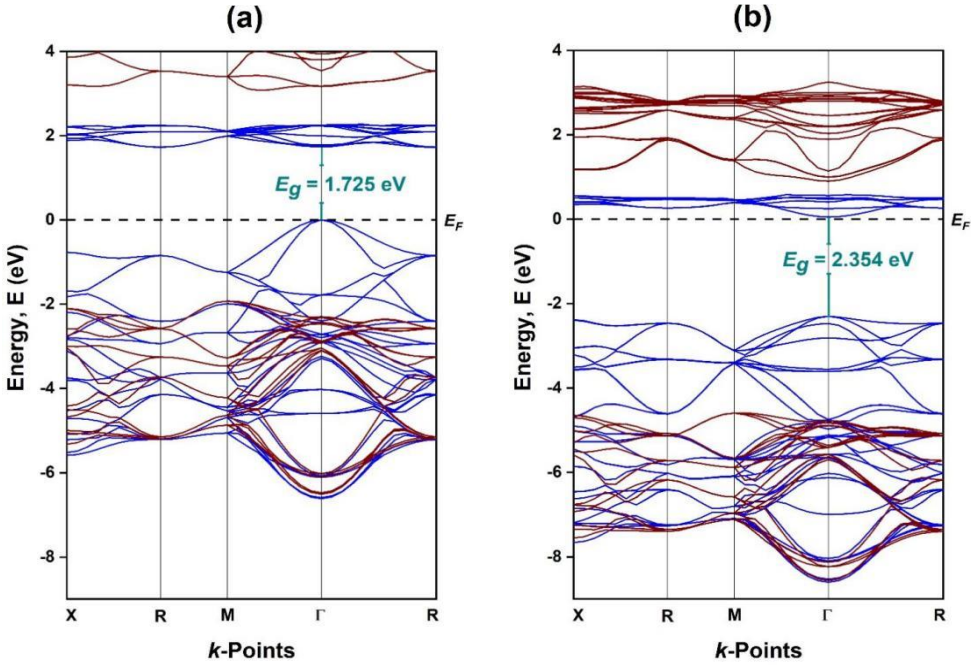

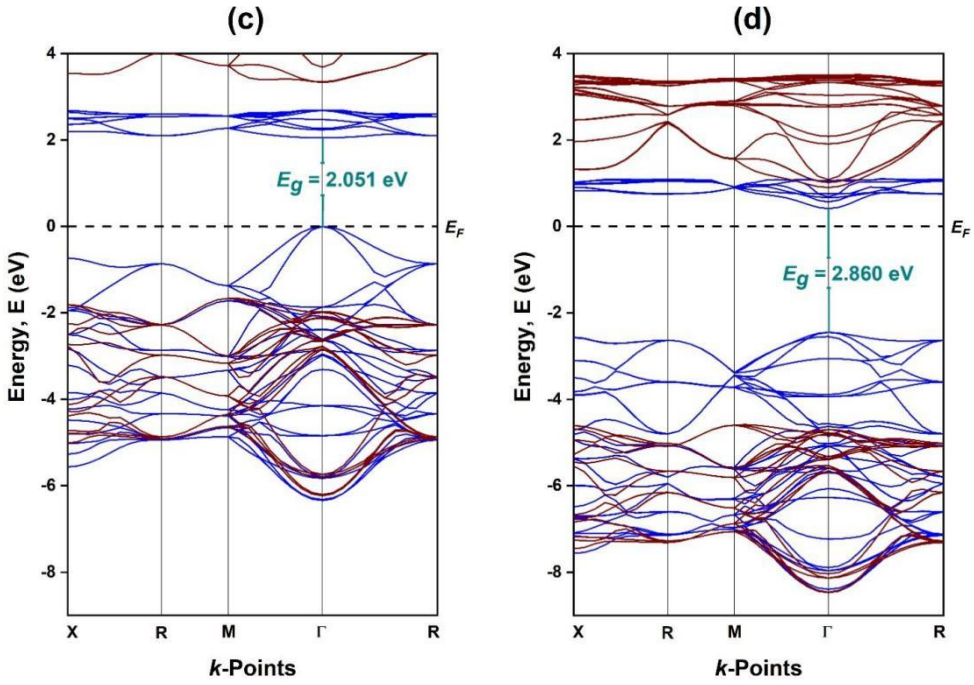

Fig. 3. Energy band diagram of UO_2 with (a) LDA+U (U=4.5 eV), (b) GGA+U (U=4.5 eV), (c) LDA+U (U=5.5 eV) and (d) GGA+U (U=5.5 eV) approximations.

Fig. 4. represents the XRD and Neutron diffraction patterns for UO_2 drawn by the Forcite Tools from Materials Studio CASTEP [13] version 8.0. As shown in Fig. 4(a), the XRD peaks (111), (200), (220), (311), (222), (400), (331), (420), and (422) can be easily indexed to UO_2 (JCPDS 41-1422). These diffraction peaks from XRD confirm the formation of the face-centered cubic (fcc) crystal structure of UO_2 (space group: $Fm\bar{3}m$) [19]. The diffraction peaks from theoretical Neutron diffraction spectra, as shown in Fig. 4(b), also indicate the fluorite type fcc crystalline UO_2 with space group $Fm\bar{3}m$ [20].

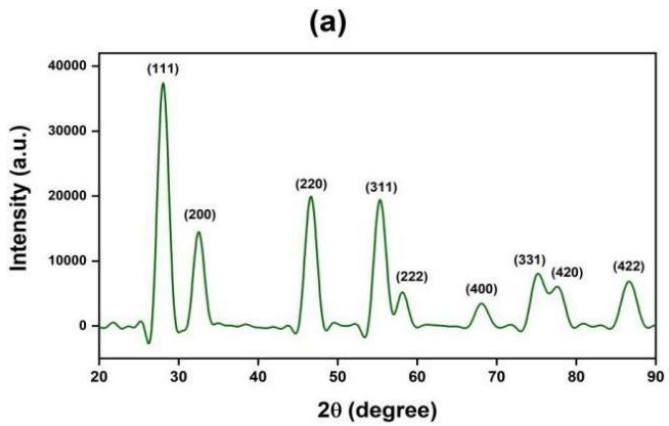

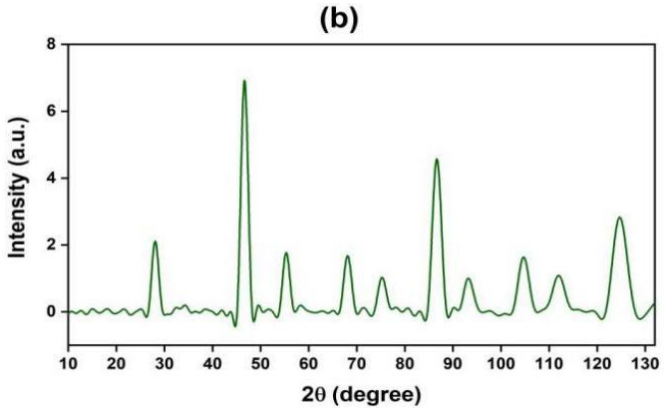

Fig. 4. (a) X-ray and (b) Neutron diffraction patterns of UO_2.

Table 3. Calculated and experimental band gap, E_g, values of UO_2.

Method	Lattice constant, a (Å)	Band gap, E_g (eV)	Electronic property	Remarks
GGA	5.475	0.000	Conductor	This work
LDA+U, U=4.5 eV	5.483	1.725	Direct band gap semiconductor/Mott-Insulator	This work
GGA+U, U=4.5 eV	5.528	2.354	Direct band gap semiconductor/Mott-Insulator	This work
LDA+U, U=5.5 eV	5.502	2.051	Direct band gap semiconductor/Mott-Insulator	This work
GGA+U, U=5.5 eV	5.623	2.860	Direct band gap semiconductor/Mott-Insulator	This work
LDA+U, U= 4.5 eV	5.490	1.700	Mott-Insulator	[1]
HSE-ACE	5.540	2.020	Mott-Insulator	[1]
GGA+U, U= 4.1 eV	5.390	1.870	Mott-Insulator	[8]
GGA+U, U= 4.5 eV	5.490	1.920	Mott-Insulator	[17]
GGA+U, U= 4.0 eV	5.550	1.800	Mott-Insulator	[18]
GGA+U, U= 4.0 eV	5.550	2.620	Mott-Insulator	[10]
Experimental	5.470	2.100±0.1	Mott-Insulator	[8,29]

3.2. *Elastic constants and thermal properties*

The elastic constants and elastic moduli of fcc UO_2 calculated from GGA-PBESOL approximation are reported in Table 4. UO_2 is found mechanically stable because the stability conditions for the cubic system are fulfilled: C_{11}-$C_{12} > 0$, $C_{11}+2C_{12} > 0$ and $C_{44} > 0$. These elastic constants and elastic moduli values are well agreed with the values obtained by Sanati *et al.* [9] and Shilpa Singh *et al.* [10]. The B/G ratio (2.25) shows that fcc UO_2 is ductile [10].

Table 4. Elastic constants (C_{11}, C_{12}, and C_{44}), Bulk modulus (B), Shear modulus (G), Young's modulus (Y), and Poisson's ratio (σ) of fcc UO_2.

Method	a (Å)	C_{11} (GPa)	C_{12} (GPa)	C_{44} (GPa)	C_{11}-C_{12} (GPa)	C_{11}+2C_{12} (GPa)	B (GPa)	G (GPa)	Y (GPa)	σ	Remarks
GGA, PBESOL	5.475	346.8	99.4	59.3	247.4	545.6	190.6	84.6	217.7	0.271	This work
GGSA	5.423	367.0	114.7	62.9	252.3	596.4	198.8	83.3	219.3	0.316	[9]
GGSA+U, U=4.5	5.548	345.7	115.5	63.4	230.2	576.7	192.2	80.6	212.1	0.316	[9]
GGA+U, U= 4.0	5.550	354.2	111.0	57.7	243.2	576.2	192.1	78.2	206.5	0.320	[10]
Experimental	5.473	389.3	118.7	59.7	270.6	626.7	209.0	83.0	221.0	0.324	[9]

The Debye temperature θ_D is a key thermal parameter linked to thermal conductivity, *k*. In this work, θ_D is calculated using elastic constants by the famous Anderson method [21]. According to this method, the Debye temperature θ_D is given by the following equation:

$$\theta_D = \frac{h}{k_B}\left[\frac{3n}{4\pi}\frac{N_A\rho}{M}\right]^{1/3} v_m$$

where, *h* is the Planck's constant, k_B is the Boltzmann constant, *n* is the number of atoms per molecule (3), N_A is Avogadro's number, ρ is the mass density (10.97 g/cm^3), *M* is the molecular weight (270.03 g/mol), and v_m is the average acoustic velocity, which can be calculated from the following equation:

$$v_m = \left[\frac{1}{3}\left(\frac{2}{v_t^3}+\frac{1}{v_l^3}\right)\right]^{-1/3}$$

where, v_t and v_l are, respectively, the transverse and longitudinal acoustic velocities, which are calculated from Shear and Bulk moduli using Navier's equations [21]:

$$v_l = \left(\frac{3B+4G}{3\rho}\right)^{1/2} \text{ and } v_t = \left(\frac{G}{\rho}\right)^{1/2}$$

The calculated Debye temperature θ_D, and average acoustic velocity, v_m are listed in Table 5. The melting temperature, T_m is calculated from the following relation [22]:

$$T_m = 553 + 5.91C_{11}$$

The calculated melting temperature, T_m for UO_2 is listed in Table 5. The minimum thermal conductivity, k_{min} is calculated by the following equation [23]:

$$k_{min} = k_B v_m \left(\frac{nN_A\rho}{M}\right)^{2/3}$$

here, k_B is the Boltzmann constant, v_m is the average acoustic velocity, *n* is the number of atoms in a molecule, N_A is Avogadro's number, ρ is the mass density, and *M* is the molecular weight. Slack's model is the utmost effective and provides the following empirical formula [24] to estimate the lattice thermal conductivity, *k* of materials:

$$k = A\frac{\delta M_{av}\theta_D^3}{\gamma^2 n^{2/3} T}$$

where, δ is the cubic root of the average atomic volume, M_{av} refers to the average atomic mass in kg/mole (M_{av}= M/n, where n is the number of atoms in the molecule) in a crystal, n denotes the number of atoms in a unit cell (12), T is the absolute temperature in K, γ is the Grüneisen parameter obtained from Poison's ratio (σ) and A is a constant ($A = 3.1 \times 10^{-6}$). The Grüneisen parameter γ can be calculated as:

$$\gamma = \frac{3(1+\sigma)}{2(2-3\sigma)}$$

The calculated values of minimum thermal conductivity, $k_{min,}$ and lattice thermal conductivity, k, are listed in Table 5. The k value at 323 K calculated from the DFT study in this work is very close to the value obtained experimentally [25-29] and theoretically [7,29] by other researchers. The variation of lattice thermal conductivity (k) using DFT calculation of UO_2 fuel as a function of temperature with a temperature range from 300 K to 2603 K is shown in Fig. 5.

Table 5. Calculated values of cubic root of average atomic volume (δ), Grüneisen parameter (γ), average acoustic velocity (v_m), Debye temperature (θ_D), melting temperature (T_m), minimum thermal conductivity (k_{min}), average atomic mass (M_{av}) and lattice thermal conductivity (k).

Method	δ(Å)	γ	v_m (km/s)	θ_D (K)	T_m (K)	k_{min} ($Wm^{-1}K^{-1}$)	M_{av} (kg/mole)	k (at 323 K) ($Wm^{-1}K^{-1}$)	Remarks
GGA, PBESOL	2.391	1.61	3.105	387	2603	1.10	90.01	8.8	This work
Experimental	-	-	-	-	-	1.70	-	9.1	[25]
Experimental	-	-	-	-	-	-	-	10.2	[26]
LDA+U,U=4.0eV	-	-	-	395	-	-	-	~11.5	[7]
Experimental	-	-	-	-	-	-	-	~8.2	[27]
Experimental	-	-	-	-	-	-	-	~6.1	[28]
GGA+U	-	-	-	-	-	-	-	~10.9	[29]
Experimental	-	-	-	-	-	-	-	~8.1	[29]

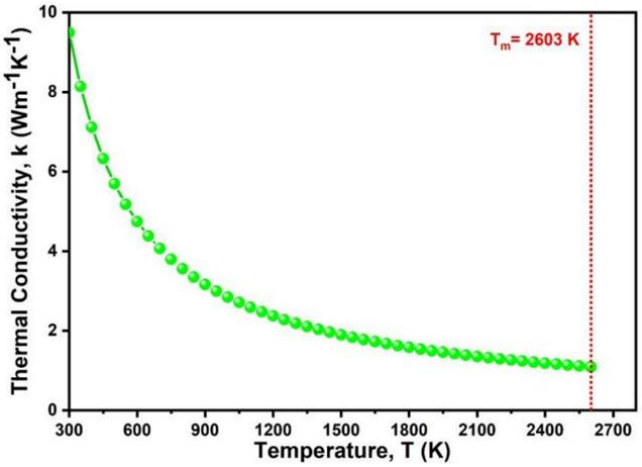

Fig. 5. Lattice thermal conductivity of the studied UO_2 solid fuel material as a function of temperature.

3.3. *Optical properties*

The optical properties of a material are measured by the interaction of photons (or incident electromagnetic waves) with that particular material surface. The response of a particular material to incident electromagnetic radiation is very significant for identifying the suitable area of optical applications such as absorbers, reflectors, conductors, coatings, and various optoelectronic device applications [27,28]. The optical parameters: (a) the complex dielectric function, ε(ω) (the real (Re) and imaginary (Im) parts), (b) refractive index η(ω) (the real (n) and imaginary (k) parts), (c) optical conductivity σ(ω) (the real (Re) and imaginary (Im) parts), (d) reflectivity R(ω), (e) absorption coefficient α(ω) and (f) loss function L(ω) of UO_2 Mott-Insulator have been calculated from LDA+U and GGA+U approximation functionals. From the frequency-dependent complex dielectric function: $\varepsilon(\omega) = \varepsilon_1(\omega) + i\varepsilon_2(\omega)$, all the other optical parameters, which are refractive index, conductivity, reflectivity, absorbance, and loss function, were calculated. The real part, $\varepsilon_1(\omega)$ of the dielectric function, ε(ω), was obtained from the imaginary part, $\varepsilon_2(\omega)$, by applying the Kramers-Kronig transformation equations. The CASTEP code evaluates the imaginary part of the dielectric function, $\varepsilon_2(\omega)$ [30,31]. The Gaussian smearing value of 0.5 eV is applied for all the optical investigations [32]. In this work, the optical properties of UO_2, along with different polarization directions ([100], [010], and [001]) for the incident electric field, have been studied. fcc UO_2 shows significant optical anisotropy for [001] polarization direction, while for [100] and [010] directions, they are isotropic for all the DFT+U calculations.

Figs. 6-10 represent the illustration of optical parameters of UO_2 measured from LDA+U and GGA+U approximation functionals with U= 4.5 and 5.5 eV. Fig. 6 shows the optical parameters measured by LDA+U (U= 4.5 eV) approximation functional. As shown in Fig. 6(a), the real (Re) and imaginary (Im) parts of the complex dielectric function, ε(ω), approach zero at ~11 eV, so that is the plasma frequency of UO_2. This calculated plasma frequency value is agreed well with the value (14 eV) obtained by J. Schoenes [33]. After this plasma frequency, UO_2 is nearly transparent, and insulator-like optical property is obtained because both the reflectivity and absorption coefficient fall sharply at 11 eV. The electric polarization is measured by the real part, and the loss of incident energy is indicated by the imaginary part of ε(ω). For UO_2, $\varepsilon_1(\omega)$ is negative for a particular energy range from 7 eV to 11 eV, indicating no polarization in this certain energy range for the incident electromagnetic fields. Although the obtained value of the dielectric constant (2.63) is found to be less than the value calculated by Schoenes [33], nevertheless, the higher value of ε(ω) makes UO_2 a suitable and potential candidate for integrated circuits [34]. The real part of the refractive index, n, the ratio between the speed of light in UO_2 and the speed of light in free space, and the extinction coefficient, k, which is related to the optical absorbance, are drawn in Fig. 6(b). For UO_2 Mott-Insulator, n is quite high for the infrared to the ultraviolet range, and it gradually diminishes at 11 eV after peaking at ~6 eV. The value of n begins to rise slightly after the plasma frequency (11 eV).

The optical conductivity, σ(ω) spectra, is shown in Fig. 6(c). The peak in the real part of σ(ω) corresponds to the peaks in the real part of the dielectric constant, $\varepsilon_1(\omega)$, and refractive index, n. The imaginary part of σ(ω) corresponds to loss and shows a close agreement with the peak positions of the imaginary part of the dielectric constant, $\varepsilon_2(\omega)$, and the imaginary part of the refractive index, which is called the extinction coefficient, k. The reflectivity, R(ω) curve as drawn in Fig. 6(d), started to rise from the infrared (0.01–2 eV) and visible light (2–3 eV) regions but from 4 eV to 10.5 eV (ultraviolet region, energy range is $3–10^3$ eV), high reflectivity is observed for UO_2. This indicates that UO_2 is an ultraviolet reflector in this particular spectral band. As shown in Fig. 6(e), the optical absorption coefficient, α(ω) spectrum shows the strong absorption phenomenon at the energy ranges of 4.5–10.5 eV and 17–25 eV. So, UO_2 is an efficient ultraviolet absorber in these two energy bands. In the loss function, L(ω) spectra, as shown in Fig. 6(f), there is a very sharp peak at the plasmon energy of the material (11 eV). This is coherent with the fall of absorbance and reflectivity curves around the same energy, and from this observation, we can conclude that UO_2 is effectively transparent to the incident photons from the plasma resonance energy and shows insulator-like optical behaviors. The same optical properties were found from the optical parameters calculations by LDA+U (U= 5.5 eV) approximation for UO_2, as shown in Fig. 8.

By GGA+U (U= 4.5 and 5.5 eV) approximations as shown in Figs. 7 and 9, the calculated optical parameters (dielectric constant, refractive index, and optical conductivity) show sharper peaks at low energies. The dielectric function, ε(ω), becomes high in the infrared energy region and decreases sharply towards the end of the visible light region. After that, ε(ω) rises and illustrates the same trends of optical response as it obtained by LDA+U (U= 4.5 and 5.5 eV) approximations for UO_2 and then approaches zero at the plasma frequency value ~11.5 eV. The high value of the dielectric constant is obtained (12.10) by GGA+U (U= 4.5 and 5.5 eV) calculations which is much higher than the value found by Schoenes [33]. The same peak values of spectral patterns are observed within 3–10 eV photon frequency for the refractive index, optical conductivity, and reflectivity with the large peaks at low frequencies. The reflectivity is now high for the infrared to visible energy region in addition to the 4–11 eV ultraviolet region with a deep dip at ~2.5 eV. The loss functions, L(ω), show a very sharp peak at 11.5 eV, which is the plasma resonance energy of the material for GGA+U (U= 4.5 and 5.5 eV) approximations.

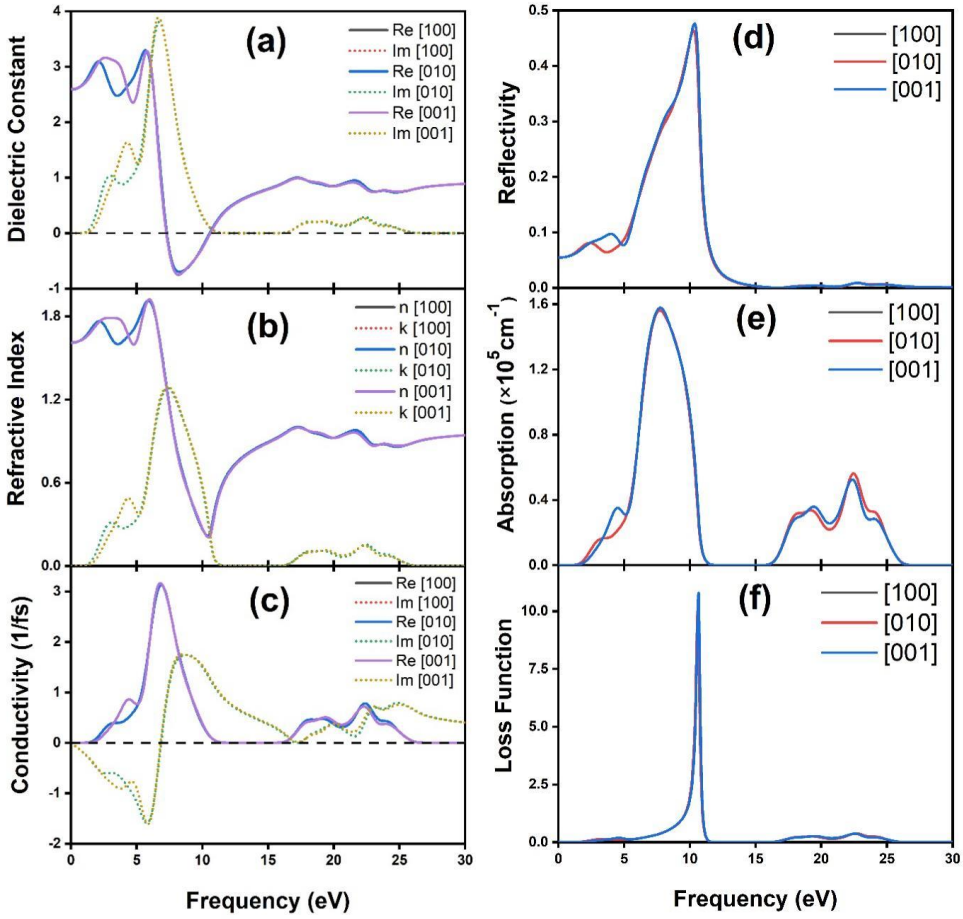

Fig. 6. The frequency dependent (a) dielectric function (real & imaginary parts), (b) refractive index (real & imaginary parts), (c) optical conductivity (real & imaginary parts), (d) reflectivity, (e) absorption coefficient and (f) loss function of UO_2 from LDA+U (U=4.5 eV) approximation.

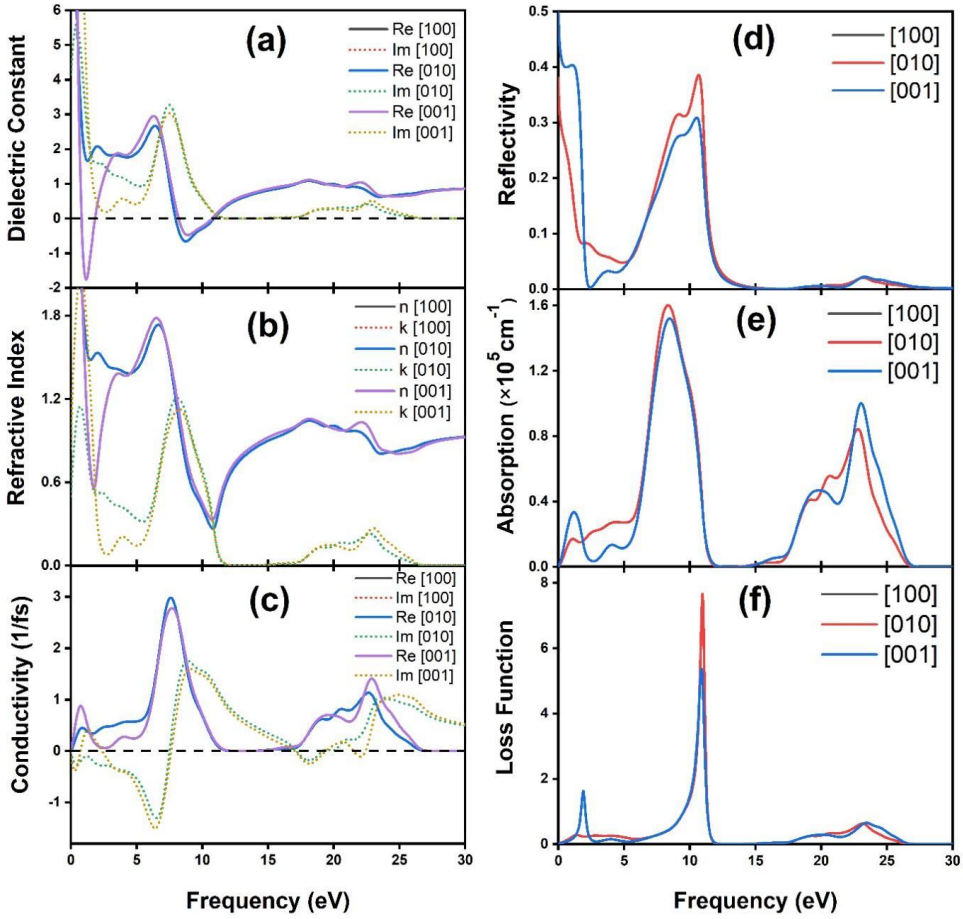

Fig. 7. The frequency dependent (a) dielectric function (real & imaginary parts), (b) refractive index (real & imaginary parts), (c) optical conductivity (real & imaginary parts), (d) reflectivity, (e) absorption coefficient and (f) loss function of UO_2 from GGA+U (U=4.5 eV) approximation.

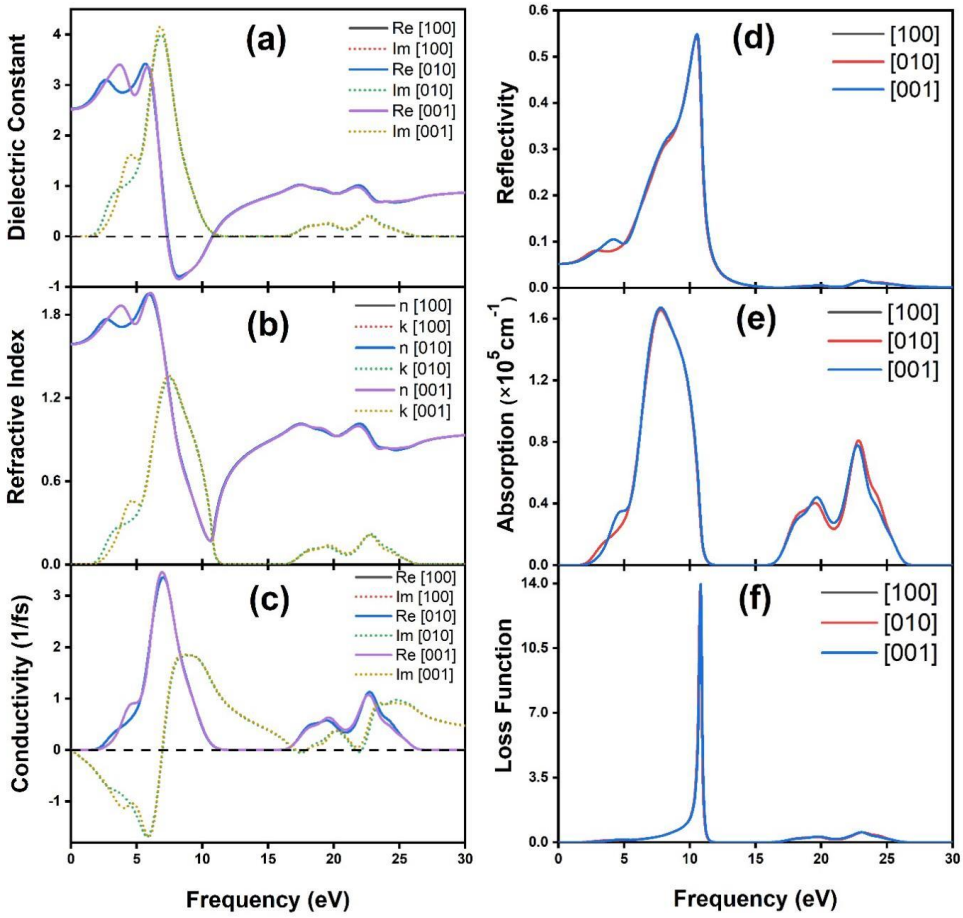

Fig. 8. The frequency dependent (a) dielectric function (real & imaginary parts), (b) refractive index (real & imaginary parts), (c) optical conductivity (real & imaginary parts), (d) reflectivity, (e) absorption coefficient and (f) loss function of UO_2 from LDA+U (U=5.5 eV) approximation.

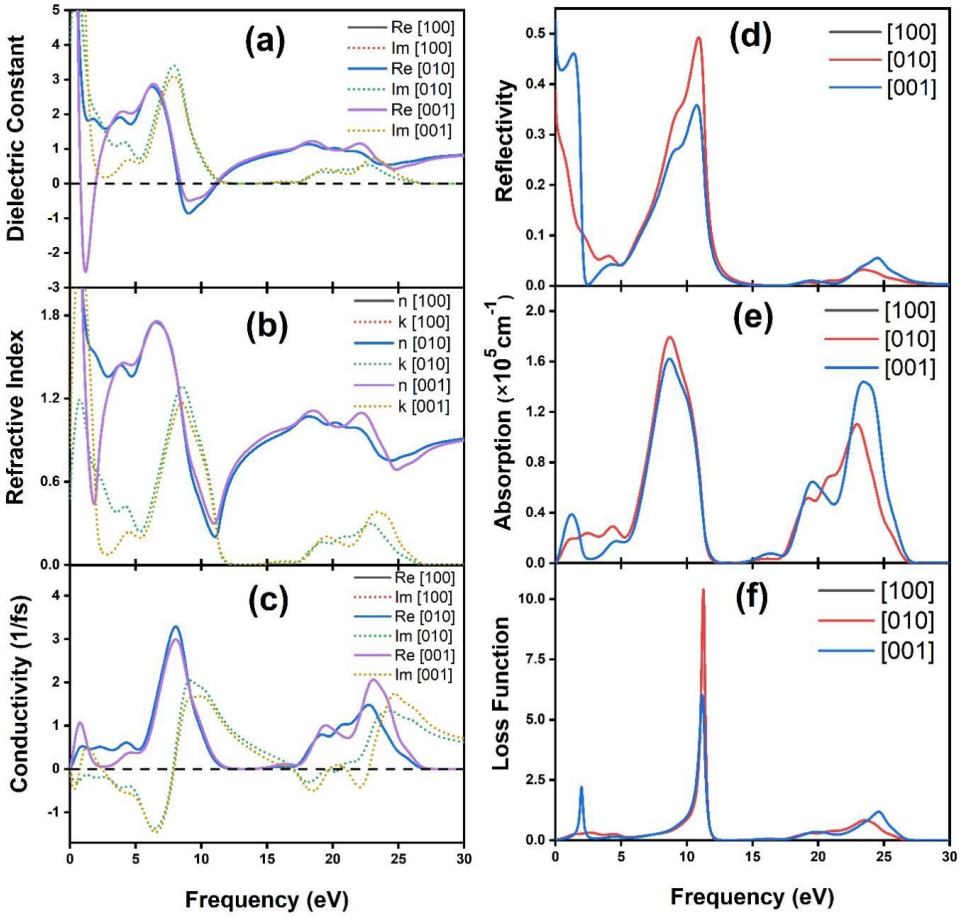

Fig. 9. The frequency dependent (a) dielectric function (real & imaginary parts), (b) refractive index (real & imaginary parts), (c) optical conductivity (real & imaginary parts), (d) reflectivity, (e) absorption coefficient and (f) loss function of UO_2 from GGA+U (U=5.5 eV) approximation.

The absorption coefficient, α(ω), as a function of the wavelength of visible light (300–800 nm) is shown in Fig. 10(a) for LDA+U and GGA+U approximation functionals with U= 4.5 and 5.5 eV. It is seen from Fig. 10(a) that UO_2 is a poor absorber of visible light and an efficient ultraviolet absorber, as we discussed before. Also, the optical band gap, the threshold energy for incident photons to be absorbed, is calculated for UO_2 by Tauc's Plot Method [35], as shown in Fig. 10(b). The calculated optical band gap, E_g for LDA+U (U= 4.5 eV), GGA+U (U= 4.5 eV), LDA+U (U= 5.5 eV) and GGA+U (U= 5.5 eV) approximations of UO_2 are 5.88, 6.69, 6.11 and 7.01 eV, respectively.

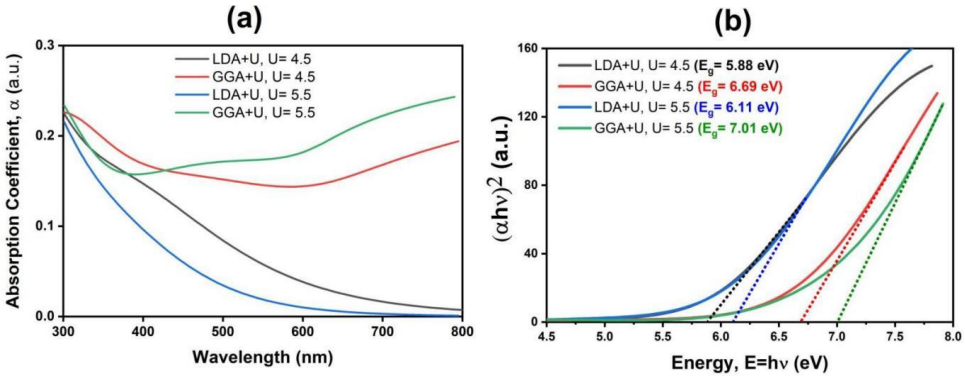

Fig. 10. (a) The absorption coefficient, α(ω) as a function of wavelength of visible light, and **(b)** Tauc's plot to calculate the optical band gap of UO_2.

4. Conclusion

By applying DFT and DFT+U based first-principles calculations, I have studied the structural, electronic, magnetic, thermal, and optical properties of fcc-structured crystalline UO_2 material. The estimated structural characteristics agreed well with the reported theoretical and experimental data. Electronic properties calculated with Hubbard U correction for strongly correlated *f* electrons show the direct band gap Mott-Insulating behavior. The obtained energy band gap values by using LDA+U and GGA+U (U= 4.5 and 5.5 eV) approximation functionals are very close to other published theoretical and experimental results. The studied UO_2 is predicted to be mechanically stable and ductile due to the fulfillment of stability conditions for the cubic system. The lattice thermal conductivity (*k*) is calculated first time by Slack's equation from elastic constants calculations with GGA-PBESOL functional, and the obtained value of *k* is agreed well with the reported values. The larger value of the optical band gap is due to the Hubbard U correction for *f-f* Mott-Insulator. The semiconducting electronic properties and higher dielectric constant make UO_2 interesting also for ultraviolet-based optical responses.

Acknowledgment

The author acknowledges the Nuclear Safety, Security and Safeguard Division, BAERA, E-12/A, Agargaon, Dhaka-1207, Bangladesh, for providing a computer facility. R. S. Sony is thankfully acknowledged for her continuous love, support, and help.

References

1. S. Sheykhi and M. Payami, Physica C: Superconductivity Its Applicat. **549**, 93 (2018). https://doi.org/10.1016/j.physc.2018.02.028
2. Y. Yun, H. Kim, H. Lim, and K. Park, J. Korean Phys. Soc. **50**, 1285 (2007). https://doi.org/10.3938/jkps.50.1285

3. J. Hubbard- Proc. of the Royal So. A: Math., Phys. Eng. Sci. **276**, 238 (1963). https://doi.org/10.1098/rspa.1963.0204
4. Y. Yun, D. Legut, and P. M. Oppeneer, J. Nuclear Mater. **426**, 109 (2012). https://doi.org/10.1016/j.jnucmat.2012.03.017
5. C. G. S. Pillai and A. M. George, J. Nuclear Mater. **200**, 78 (1993). https://doi.org/10.1016/0022-3115(93)90011-M
6. H. Shi, M. Chu, and P. Zhang, J. Nuclear Mater. **400**, 151 (2010). https://doi.org/10.1016/j.jnucmat.2010.02.024
7. B.-T. Wang, J.-J. Zheng, X. Qu, W.-D. Li, and P. Zhang, J. Alloys Compds. **628**, 267 (2015). https://doi.org/10.1016/j.jallcom.2014.12.204
8. Q. Chen, X. Lai, T. Tang, B. Bai, *et al.*, J. Nuclear Mater. **401**, 118 (2010). https://doi.org/10.1016/j.jnucmat.2010.04.007
9. M. Sanati, R. C. Albers, T. Lookman, and A. Saxena, Phys. Rev. B **84**, ID 014116 (2011). https://doi.org/10.1103/PhysRevB.84.014116
10. S. Singh, Y. Sonvane, K. A. Nekrasov, A. S. Boyarchenkov, *et al.*, Solid State Sci. **132**, 106968 (2022). https://doi.org/10.1016/j.solidstatesciences.2022.106968
11. J. T. Pegg, A. E. Shields, M. T. Storr, A. S. Wills, D. O. Scanlon, and N. H. de Leeuw, Phys. Chem. Chem. Phys. **21**, 760 (2019). https://doi.org/10.1039/c8cp03581d
12. S. L. Dudarev, D. N. Manh, and A. P. Sutton, Philosophical Magazine B **75**, 613 (1997). https://doi.org/10.1080/13642819708202343
13. S. J. Clark, M. D. Segall, C. J. Pickard, P. J. Hasnip, *et al*., Zeitschrift fuer Kristallographie, **220**, 567 (2005). https://doi.org/10.1524/zkri.220.5.567.65075
14. H. J. Monkhorst and J. D. Pack, Phys. Rev. B, **13**, 5188 (1976). https://doi.org/10.1103/PhysRevB.13.5188
15. M. Islam, M. S. I. Sarker, T. Nakamura, M. K. R. Khan, *et al*., Mater. Chem. Phys. **269**, 124727 (2021). https://doi.org/10.1016/j.matchemphys.2021.124727
16. T. Cardinaels, K. Govers, B. Vos, S. V. den Berghe, *et al.*, J. Nuclear Mater. **424**, 252 (2012). https://doi.org/10.1016/j.jnucmat.2012.02.025
17. P. Nerikar, T. Watanabe, J. S. Tulenko, S. R. Phillpot, and S. B. Sinnott, J. Nuclear Mater. **384**, 61 (2009). https://doi.org/10.1016/j.jnucmat.2008.10.003
18. F. Gupta, G. Brillant, and A. Pasturel, Philosophical Magazine **87**, 2561 (2007). https://doi.org/10.1080/14786430701235814
19. Q. Wang, G.-D. Li, S. Xu, J.-X. Li, and J.-S. Chen, J. Mater. Chem. **18**, 1146 (2008). https://doi.org/10.1039/B716990F
20. L. Desgranges, G. Baldinozzi, G. Rousseau, J. -C. Niepce, and G. Calvarin, Inorg. Chem. **48**, 7585 (2009). https://doi.org/10.1021/ic9000889
21. O. L. Anderson, J. Phy. Chem. Solids, **24**, 909 (1963). https://doi.org/10.1016/0022-3697(63)90067-2
22. M. E. Fine, L. D. Brown, and H. L. Marcus, Scripta Metallurgica **18**, 951 (1984). https://doi.org/10.1016/0036-9748(84)90267-9
23. D. R. Clarke, Surf. Coatings Technol. **164**, 67 (2003). https://doi.org/10.1016/S0257-8972(02)00593-5
24. D.T. Morelli and G. A. Slack, High Lattice Thermal Conductivity Solids. In, Edited by S. L. Shindé and J. S. Goela, High Thermal Conductivity Materials (Springer, New York, NY, 2006). https://doi.org/10.1007/0-387-25100-6_2
25. J. T. White and A. T. Nelson, J. Nuclear Mater. **443**, 342 (2013). https://doi.org/10.1016/j.jnucmat.2013.07.063
26. P. B. Weisensee, J. P. Feser, and D. G. Cahill, J. Nuclear Mater. **443**, 212 (2013). https://doi.org/10.1016/j.jnucmat.2013.07.021
27. J. Bates, Thermal diffusivity of UO_2, Ceramics Research and Development Quarterly Report, July-September (BNWL-198, Richland, WA, 1965)
28. R. L. Gibby, J. Nuclear Mater. **38**, 163 (1971). https://doi.org/10.1016/0022-3115(71)90040-7

29. J. W. L. Pang, A. Chernatynskiy, B. C. Larson, W. J. L. Buyers, *et al*., Phys. Rev. B **89**, ID 115132 (2014). https://doi.org/10.1103/PhysRevB.89.115132
30. A. Chakraborty, M. N. H. Liton, M. S. I. Sarker, M. M. Rahman, and M. K. R. Khan, Physica B: Condensed Matter **648**, ID 414418 (2023). https://doi.org/10.1016/j.physb.2022.414418
31. N. S. Khan, B. R. Rano, I. M. Syed, R. S. Islam, and S. H. Naqib, Results in Physics, **33**, 105182 (2022). https://doi.org/10.1016/j.rinp.2022.105182
32. M. S. Ali, M. A. Rayhan, M. A. Ali, R. Parvin, and A. K. M. A. Islam, J. Sci. Res. **8**, 109 (2016). https://doi.org/10.3329/jsr.v8i2.25057
33. J. Schoenes, J. Appl. Phys. **49**, 1463 (1978). https://doi.org/10.1063/1.324978
34. H. Shi M. Chu, and P. Zhang, J. Nucl. Mater. **400**, 151 (2010). https://doi.org/10.1016/j.jnucmat.2010.02.024
35. J. Tauc, R. Grigorovici, and A. Vancu, Phys. Status Solidi B **15**, 627 (1966). https://doi.org/10.1002/pssb.19660150224